7 (2025) 100122

Contents lists available at ScienceDirect

Chemistry of Inorganic Materials

journal homepage: www.elsevier.com/locate/cinorg

Magnetized retrieve of Ag–TeO_3/Fe_3O_4@TiO_2 hybrid nanocomposites for optical, kinetically, half-life period and its photocatalytic assessment of methylene blue and methyl orange dyes

A. Anbu [a,*], M. Dilipkumar [a], K. Jeyajothi [b], M. Rajasimman [a], M.S. Manojkumar [c,**]

[a] Department Chemical Engineering, Annamalai University, Annamalai Nagar, Chidambaram, TN, India
[b] Department Petrochemical Engineering, Mahendra Institute of Engineering and Technology, Mahendra Puri, Mallasamudram (W), Thiruchengode, Namakkal-DT, TN, India
[c] Department of Biotechnology, Vivekanandha College of Engineering for Women (Autonomous), Elayampalam, Namakkal, 637210, TN, India

ARTICLE INFO

Keywords:
Ag–TeO_3/Fe_3O_4@TiO_2 NCs
Photocatalyst
Capsicum frutescence fruit
BET isotherm
Half-life period

ABSTRACT

The present research effectively constructed a core-shell-shell structure of Ag–TeO_3/Fe_3O_4@TiO_2 utilizing *Capsicum frutescence extract*, which is both magnetized highly recoverable. The catalyst was applied to photo catalytically degrade the colorants methyl orange (MO) and methylene blue (MB). The catalyst's function was further examined using XRD, FTIR, SEM, TEM/HRTEM, VSM, BET isotherm and UV–Visible spectroscopic analysis. Thus, Ag–TeO_3/Fe_3O_4@TiO_2 exhibited magnetized characteristics, including a saturation magnetic of 51.9 emu/g and a bandwidth value of 2.5 eV and half life period of 91.9min^{-1}. The photocatalytic breaking down of MO and MB dyes mirrored the Langmuir-Hinshelwood pattern. Breakdown could be observed at the MO and MB dyes after 45 and 50 min of radiation exposure, with MO and MB dye elimination efficiencies reaching 99.2 % and 98.2 %, correspondingly. Following five attempts of regenerating Ag–TeO_3/Fe_3O_4@TiO_2 demonstrated 96.96 % MO and MB dye elimination performance.

1. Introduction

The use of various industrial chemicals, including organic dyes, spans numerous industries such as pharmaceuticals, plastics, paints, textiles, food production, and agriculture. However, when organic dyes are present in water at concentrations exceeding 1 mg/L, they create significant environmental and health challenges due to their chemical resilience and difficulty to degrade. One such example is methylene blue ($C_{16}H_{18}CN_3S$ Cl), a cationic aromatic compound commonly employed as a dye. Its release into ecosystems deteriorates water quality and presents health hazards, including skin and eye irritation, as well as impacts on vital organs such as the kidneys, liver, and brain, alongside effects on the central nervous and reproductive systems [1–5].

Several methods have been developed to remove methylene blue from wastewater, including techniques like ozonation, ultrafiltration, chemical coagulation, and photocatalysis. Among these, photocatalysis is particularly noteworthy due to its simplicity and eco-friendliness, especially when solar energy serves as the light source [6–9] The efficiency of photocatalysis depends on factors such as the photocatalyst's bandgap energy, surface area, light absorption capacity, and operational variables like pH and temperature [10].

Titanium dioxide (TiO_2) is one of the most extensively studied photocatalysts, owing to its strong oxidative potential, non-toxic nature, affordability, and stability [11]. It naturally occurs in forms like anatase and rutile, which undergo phase changes at specific temperatures. However, TiO_2 also has drawbacks, including its wide energy bandgap that necessitates UV light for activation and a high recombination rate of electron-hole pairs, limiting its efficiency [12]. To overcome these limitations, doping TiO_2 with metals such as Fe or Ag has been investigated. Studies have shown that metal-doped TiO_2 improves photocatalytic performance by altering its structural and electronic properties, though results vary based on the synthesis process and experimental setup. Silver (Ag) and tellurite (TeO_3) were incorporated into the Fe_3O_4@TiO_2 system to address the inherent limitations of pure TiO_2, particularly its wide bandgap and high electron–hole recombination rate. Ag plays a crucial role as an electron sink, suppressing charge

* Corresponding author.
** Corresponding author.
E-mail addresses: anbuchemical4@gmail.com (A. Anbu), msmanojkumar1987@gmail.com (M.S. Manojkumar).

https://doi.org/10.1016/j.cinorg.2025.100122
Received 10 May 2025; Received in revised form 24 September 2025; Accepted 26 September 2025
Available online 27 September 2025
2949-7469/© 2025 Published by Elsevier B.V. This is an open access article under the CC BY-NC-ND license (http://creativecommons.org/licenses/by-nc-nd/4.0/).

recombination and prolonging the lifespan of photogenerated carriers. Additionally, the surface plasmon resonance (SPR) effect of Ag nanoparticles improves visible-light absorption, extending the photocatalytic response beyond the UV spectrum. In parallel, TeO_3 introduces defect states within the bandgap, which reduces the effective bandgap energy and promotes efficient charge separation and migration across the semiconductor interfaces. The combined effect of Ag and TeO_3 enhances light harvesting, minimizes recombination losses, and accelerates the generation of reactive oxygen species (ROS). As a result, Ag–TeO_3 serves as an effective cocatalyst system for modifying TiO_2, leading to superior photocatalytic degradation of persistent dyes like methylene blue and methyl orange under solar irradiation.

Capsicum frutescence, sometimes known for its sweet chilies, is a Solanaceae genus. Capsicum peppers' powerful flavor is presumably caused by a mixture of seven related alkaloids compounds, one of the most frequent of which is capsaicin. The molecules responsible for the spicy flavor are capsicum alkaloids components [13–15]. They have the potential of having a profound psychological impact and are being identified for their medicinal, cognitive abilities and nutritional properties. While ingested in modest dosages in the usual diet, they considerably reduce bloodstream, cardiovascular disease, and pulmonary lipid levels. due to the fact this fruit extracts contains various secondary metabolic byproducts; it is thought to have the potential to perform as a good metallic ion inhibiting and stabilization drug. We describe the creation of Ag–TeO_3/Fe_3O_4@TiO_2 hybrid nanocomposite through the reduction of metallic ions utilizing C. frutescence fruity aquatic extract in this effort [16].

Recent advancements emphasize the development of hybrid Nano catalysts, such as Ag–TeO_3/Fe_3O_4@TiO_2 produced using *Capsicum frutescence* extract by environmentally sustainable methods. These innovative materials have demonstrated significant effectiveness in degrading dyes like methyl orange and methylene blue under UV irradiation and their photocatalytic activity is closely tied to their structural and compositional features and also half -life period was discussed.

2. Materials and methods

2.1. Sources

The investigation utilized high-purity chemical reagents: titanium tetra butoxide ($Ti(OC_4H_9\text{-}n)_4$, 98 %), iron(III) nitrate ($Fe(NO_3)_3{\cdot}9H_2O$, 99 %), silver nitrate ($AgNO_3$), and sodium tellurite ($NaTeO_3$).And synthetic dyes Methyl orange ($C_{14}H_{14}N_3NaO_3S$), Methylene blue ($C_{16}H_{18}ClN_3S$) dyes were from received from precision scientific & co. All materials were certified for quality and obtained from Sigma Aldrich chemicals PVT.Ltd., Tamilnadu, India. All the experiments were carried out without any purifications.

2.2. Preparation of Capsicum frutescence fruit extract

The fruits of *Capsicum frutescence* were methodically cleaned using filtered water to remove any contaminants or impurities. After air drying outdoors, the fruits were chopped into smaller segments. A total of 25 g of the chopped fruits was placed in a capped glass bottle with 100 mL of deionized water. The mixture was heated for approximately 30 min, then allowed to cool at room temperature [17]. The cooled extract was filtered using Whatman filter paper No. 1.

2.3. Synthesis of Fe_3O_4/TiO_2 nanocomposites (NCs)

The nanocomposites were prepared through a magnetically stirred synthesis process. Gradually, 20 mL of the prepared Capsicum frutescence extract was added to a container with 50 mL of titanium tetra butoxide dissolved in Milli-Q water. Subsequently, 30 mL of iron (III) nitrate solution was incorporated. The resulting clear solution underwent ultrasonic treatment for 2 h to produce a milky slurry [18] This slurry was transferred into a titanium sterilizer and heated at 400 K for 3 h. Afterward, centrifugal separation was employed to isolate byproducts from the primary solution. The residues were washed with distilled water and ethanol thrice, then air-dried in an oven at 273 K for 6 h.

2.4. Formation of Ag–TeO_3/Fe_3O_4@TiO_2 nanocomposites

To prepare the hybrid Ag–TeO_3/Fe_3O_4@TiO_2 composites (1.0 wt% Ag), 0.8 mg of Fe–TiO_2 nanomaterials was mixed with specific quantities of silver nitrate and sodium tellurite dissolved in 50 mL of deionized water, combined with 20 mL of *Capsicum frutescence extract* [19] This mixture was stirred for 1 h at room temperature and subsequently exposed to UV light for 3 h. The resulting nanocomposites were separated via centrifugation and rinsed with distilled water and ethanol. Finally, the composites were dried in a furnace at 150 °C for 3 h and subjected to sterilization at 450 °C for 1 h. The similar manner for synthesis of Ag–TeO_3 and Fe_3O_4 Nanoparticles respectively.

2.5. Photocatalysis test

The photocatalytic experiments were performed in aqueous solutions under UV light, utilizing a 400 W mercury lamp emitting light at a wavelength of 365 nm, with each test lasting up to 120 min [20]. A fixed quantity of 10 mg of Ag–TeO_3//Fe_3O_4@TiO_2 composite particles was introduced into the solutions, while the initial concentrations of Methylene blue (MB) and Methyl orange (MO) dyes varied between 10 ppm and 20 ppm. The pH of the solutions was adjusted using either HCl or NaOH, and the temperature was kept constant at 30 °C with the help of a circulating water pump throughout the UV exposure period. Before initiating UV irradiation, the solutions were kept in darkness for 30 min to establish an adsorption-desorption equilibrium. During the reaction, samples were collected at regular intervals, centrifuged to separate the composite particles, and the resulting supernatant was promptly analyzed using UV–visible spectrophotometry (Lambda 800, PerkinElmer, U.S.A.). This analysis monitored absorption changes over a wavelength range of 200–900 nm, focusing on characteristic peaks at 662 nm for MB and 463 nm for MO. Changes in absorption intensities were compared to previously established calibration curves to determine the remaining concentrations of MB and MO in the solutions. After the experiments, some of the composite particles were retrieved using an external magnet, thoroughly cleaned with water and ethanol, and subsequently reused as catalysts under identical UV exposure conditions for additional trials.

2.6. Analytical characterization

The composite particles' microstructure was examined with field-emission scanning electron microscopy (FE-SEM, JSM-6700F, JEOL, Japan) and transmission electron microscopy (TEM, JEM-2010, JEOL, Japan). X-ray diffraction (XRD, MAC MXP III, Japan) with Cu Kα radiation at a wavelength of 1.5406 Å was used to determine the crystalline structure. The zeta potential of the particles was measured using laser Doppler electrophoresis (Nano ZS, Malvern Instruments, U.K.) in water with a pH range from 2 to 12, adjusted with HCl and KOH. Nitrogen gas adsorption–desorption analysis (ASAP 2020, Micromeritics, U.S.A.) at liquid nitrogen temperature (77.4 K) was employed to evaluate the pore structure and specific surface area of the composite particles. The pore size distribution was calculated from the adsorption branch of the isotherm using the Barrett–Joyner–Halenda (BJH) method. The magnetic properties of the composite nanoparticles were analyzed using a superconducting quantum interference device (SQUID, MPMS, Quantum Design, U.S.A.), measuring their response within a magnetic field range of −20 to +20 kOe at 25 °C.

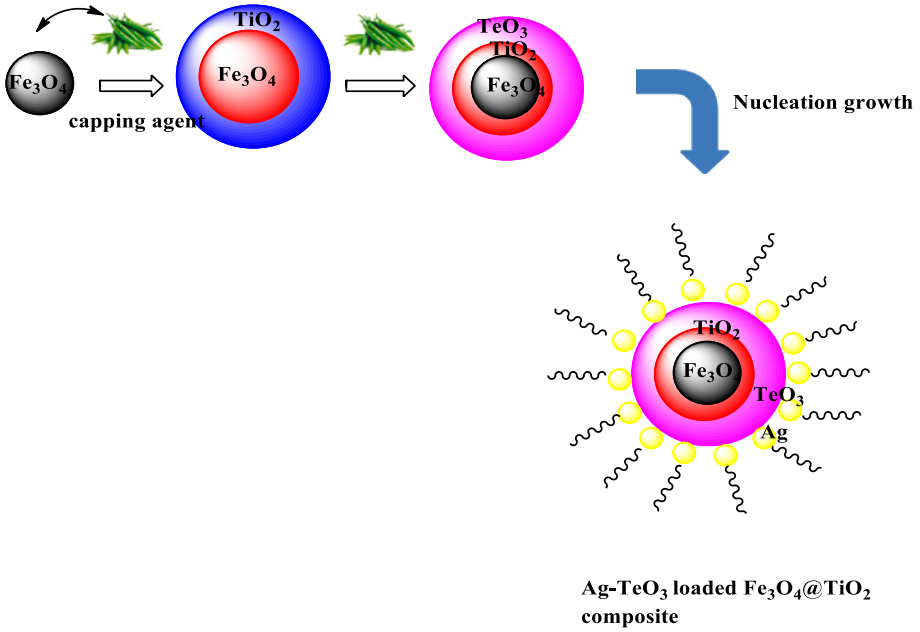


Fig. 1. schematic representation of Ag–TeO_3 NPs loaded on Fe_3O_4/TiO_2 nano Surface.

3. Results and discussion

3.1. Formation of nanocomposites

Formation of the core–shell–shell Ag–TeO_3/Fe_3O_4@TiO_2 nanocomposite using *Capsicum frutescence* extract is governed by redox chemistry and biomolecular stabilization. Fe_3O_4 nanoparticles are first synthesized as the magnetic core due to their high saturation magnetization and stability, which enables simple recovery from aqueous media. A TiO_2 shell is then coated over Fe_3O_4 through controlled hydrolysis and condensation, forming Fe_3O_4@TiO_2, where TiO_2 provides photocatalytic stability and surface anchoring sites. When Ag^+ and Te^{6+} ions are introduced into the *C. frutescence* extract, phytochemicals such as polyphenols and flavonoids donate electrons, reducing Ag^+ to Ag^0 and Te^{6+} to TeO_3^{2-}. These reduced species nucleate and grow on the Fe_3O_4@TiO_2 surface, while other functional groups in the extract (–OH, –COOH, $–NH_2$) coordinate to metal centers, acting as capping and stabilizing agents. This bio-reduction process directs the uniform deposition of Ag–TeO_3 as the outer shell, yielding a hierarchical core–shell–shell structure. The scientific rationale behind this architecture lies in the synergistic effects: Fe_3O_4 imparts magnetism and recoverability, TiO_2 ensures chemical robustness and photocatalytic activity, while Ag–TeO_3 enhances visible-light absorption, electron–hole separation, and reactive oxygen species (ROS) generation. This integrated mechanism results in a multifunctional nanocomposite with superior photocatalytic efficiency for dye degradation.

3.2. XRD analysis

The X-ray diffraction (XRD) method was employed to analyse the phases, quality, and crystalline structure of the catalyst. Fig. 2 presents the XRD patterns of as synthesized Ag/TeO_3 NPs and Ag–TeO_3/Fe_3O_4@TiO_2 NPs. All the synthesized show anatase as the dominant phase. The notable diffraction peaks observed at 25.4°, 37.9°, 48.2°, 54°, 55.2°, and 62.9° correspond to the (101), (004), (200), (105), (211), and (204) crystal planes, respectively, supported by the JCPDS 21–1272 standard. The XRD patterns suggest that the crystalline structure of TiO_2 remains stable during activation, in line with results from similar research [21]. Peaks at 44.6° (400), 54° (422), and 62.8° (440) are assigned to Fe_3O_4 diffraction patterns (JCPDS 65–3107). When silver

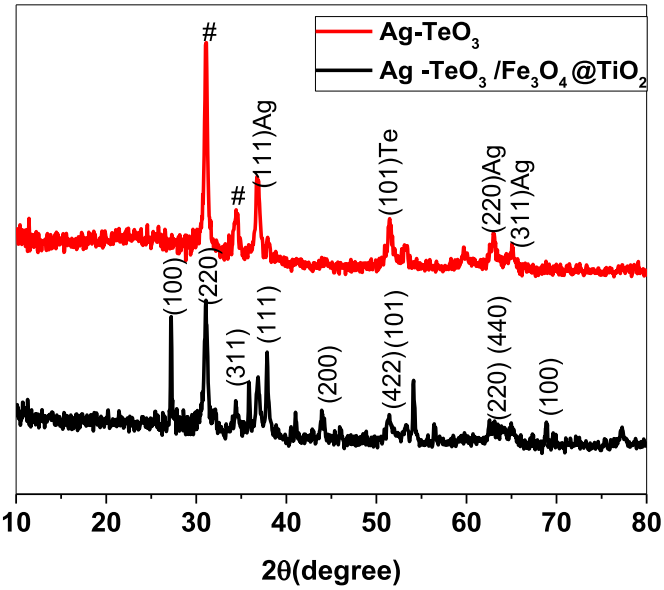


Fig. 2. XRD pattern of synthesized Ag/TeO_3 NPs and Ag–TeO_3/Fe_3O_4@-TiO_2 NPs.

ions are added to the Fe_3O_4–TiO_2 nanocomposite crystalline structure, new peaks appear at 38.7° (111), 44.5° (200), and 62.9° (220), indicating the presence of silver, according to JCPDS 04–0783. The crystalline structure of Fe_3O_4–TiO_2 nanoparticles changes with increasing Fe content, as higher Fe concentration significantly affects the strength of the TiO_2 crystalline structure. Despite these changes, the distinctive anatase peak of TiO_2 remains unchanged in all samples, with no detectable shifts in the peaks. Additionally, no extra Fe_3O_4 diffraction peaks were found, suggesting that Fe_3O_4 is evenly distributed in very low concentrations on the TiO_2 substrate [22].

The Scherrer equation was used to estimate the average crystallite sizes based on the prominent (101) anatase peak at $2\theta = 25.4°$ [23]. The average crystallite sizes were calculated as 23.2 nm, 19.2 nm, for samples (a), and (b), respectively. All samples showed similar diffraction patterns; however, sample (c) exhibited a smaller average crystallite size

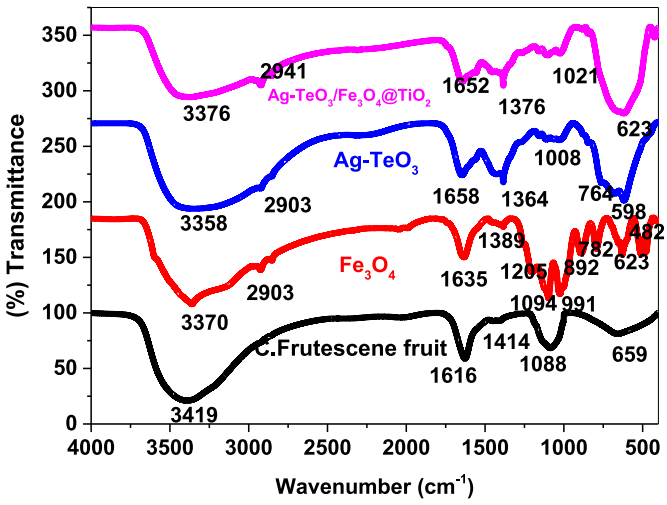


Fig. 3. FTIR spectrum of synthesized Fe_3O_4 NPs, Ag–TeO_3 NPs and Ag–TeO_3/Fe_3O_4@TiO_2 NCs.

than the others. Fig. 1 does not show all peaks related to Fe and Ag due to their low concentrations, which are below the detection limit of XRD. The Scherrer formula was employed to determine the average crystalline sizes

$$D = 0.9\,\lambda / \beta Cos\theta \quad (1)$$

where λ represents the X-ray wavelength, β denotes the full width at half maximum (FWHM) of the diffraction peak, and θ is the diffraction angle. Using this method, the average crystalline sizes of Ag–TeO_3 and Ag–TeO_3/Fe_3O_4@TiO_2 were calculated to be 24 nm and 18 nm, respectively.

3.3. FTIR analysis

Fig. 3 presents the FTIR spectra of *Capsicum frutescence* fruit extract, Fe_3O_4 nanoparticles, Ag–TeO_3 nanoparticles, and Ag–TeO_3/Fe_3O_4@-TiO_2 nanocomposites synthesized using a green method. The broad absorption observed at 3419–3376 cm^{-1} in both the extract and nanocomposites corresponds to O–H stretching of hydroxyl and phenolic groups, signifying the participation of phytochemicals in nanoparticle reduction and stabilization. The peaks around 2903–2941 cm^{-1} indicate aliphatic C–H stretching vibrations, while the sharp band near 1635–1652 cm^{-1} is linked to C═O stretching of amide groups, suggesting protein binding on the nanoparticle surface. Absorptions at 1376–1389 cm^{-1} are attributed to C–N stretching of amines, and those within 1021–1088 cm^{-1} confirm C–O stretching of alcohol and carboxyl moieties. A distinct Fe–O stretching band detected at 623–659 cm^{-1} in Fe_3O_4 and its composites verifies the spinel phase formation. For Ag–TeO_3, characteristic peaks between 1008 and 1364 cm^{-1} correspond to Te–O and Ag–O bonds. In the hybrid Ag–TeO_3/Fe_3O_4@TiO_2 nanocomposite, additional bands at 764–482 cm^{-1} arise from Ti–O–Ti stretching, confirming the integration of TiO_2. Overall, the findings indicate that the biomolecules in *C. frutescence* extract serve as natural reducing and capping agents, ensuring stability and functionalization of the synthesized nanocomposites [24].

3.4. UV–visible absorbance spectrum

Fig. 4 depicts the ultraviolet–visible spectrum of Fe_3O_4, Ag–TeO_3 NPs and Ag–TeO_3/Fe_3O_4@TiO_2 NCs hybrid photosynthetic catalyst revealing several similar characteristics within the wavelength region exceeding 477 nm, in spite of the substrate displaying major absorption at this specific wavelength [25]. Typical Ag–TeO_3 band exhibits considerable absorbing around 417 nm, which corresponds to the conventional TiO_2 absorbing the brink, yet there is little uptake beyond 477 nm. whereas the color spectrum correlating to the Ag–TeO_3/Fe_3O_4@TiO_2 material displays a wide penetration throughout the complete optical bandwidth, which has been documented in the available literature. The bandwidth ratio was found through graphing $(\alpha h\nu)^2$ vs. hν (Fig. 4 (b). Fe_3O_4 bandwidth of 3.1 eV, Ag–TeO_3 bandwidth of 2.7 eV was attained, as well as covering Ag–TeO_3 with Fe_3O_4@TiO_2 reduced the bandwidth. thereby, Ag–TeO_3/Fe_3O_4@TiO_2 exhibits a bandwidth of 2.5 eV.

3.5. BET analysis

The N_2 adsorption-desorption analysis revealed that the catalysts possessed a nanoporous structure in Ag–TeO_3//Fe_3O_4@TiO_2. Fig. 5(a) highlights that the prepared catalysts exhibited mesoporous characteristics due to their type IV isotherms, as per the Barrett-Joyner-Halenda model. The pore structures of Ag–TeO_3/Fe_3O_4@TiO_2 were predominantly around 18 nm in size. Additionally, the S_{BET} values for the nanospherical framework were found to be 82.4 m^2/g, respectively, based on adsorption data. This phenomenon was attributed to the partial blockage of TiO_2 pore spaces by metal oxides, facilitated by both chemical and physical interactions [26].

3.6. Magnetic properties

Fig. 6 graphic displays the magnetic attraction patterns of Fe_3O_4 and

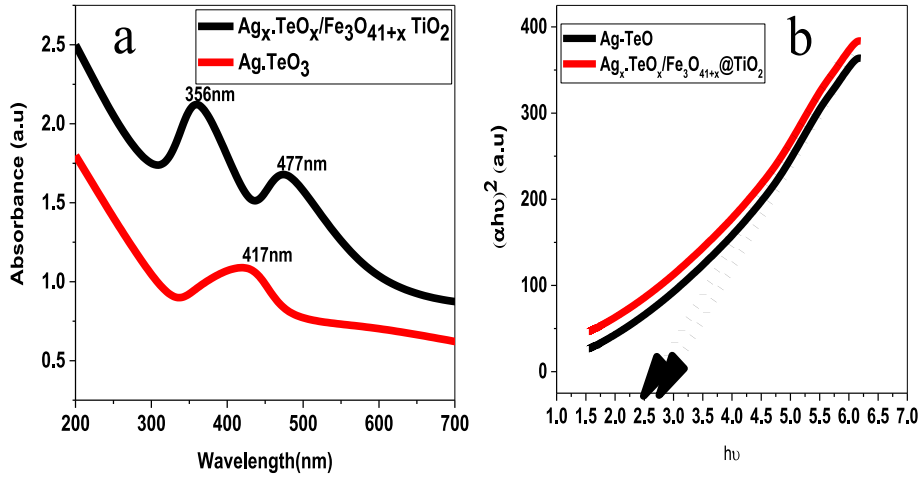


Fig. 4. represents UV–Visible spectrum (b) tauc graph of synthesized Fe_3O_4, Ag–TeO_3 NPs and Ag–TeO_3/Fe_3O_4@TiO_2 NCs using *Capsicum frutescence fruit* extract.

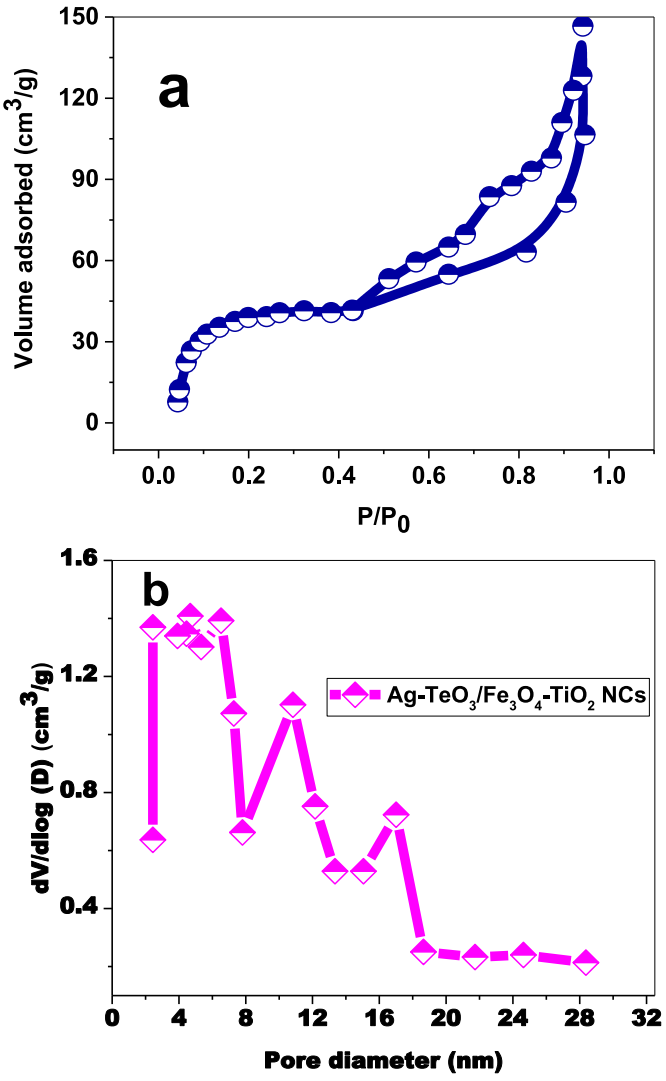


Fig. 5. (a) BET surface (b) BJH analysis of Ag–TeO_3/Fe_3O_4@TiO_2

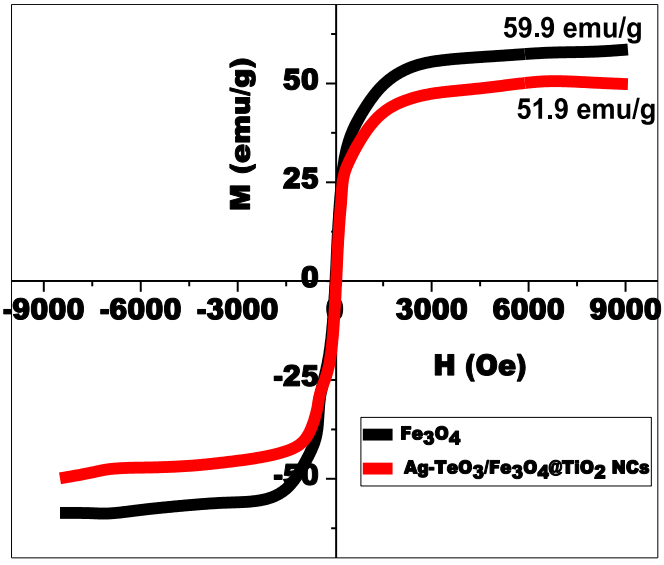


Fig. 6. VSM analysis of Fe_3O_4 NPs and Ag–TeO_3/Fe_3O_4@TiO_2 NCs.

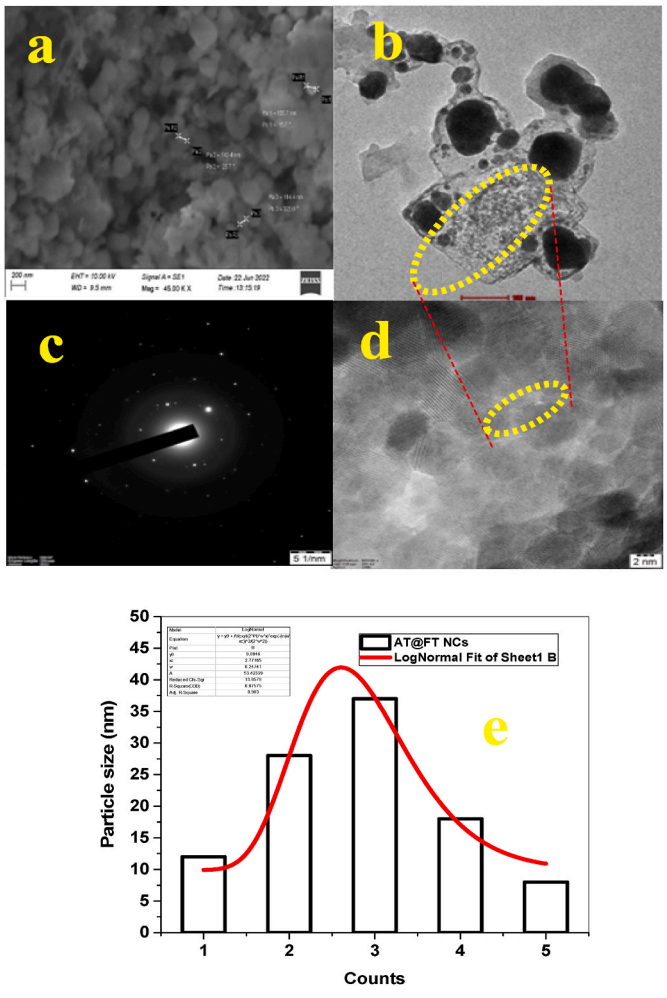


Fig. 7. (a) SEM analysis (b) TEM frame work (c) SAED arrangement (d) HRTEM micro-structural analysis (e) particle size distribution.

Ag–TeO_3/Fe_3O_4@TiO_2 created by VSM. The saturated magnetization of Fe_3O_4 is 59.9 emu/g, Furthermore, the point of saturation magnetism of Fe_3O_4 and Ag–TeO_3/Fe_3O_4@TiO_2 are 59.9 emu/g and 51.9 emu/g, correspondingly, which is less than the Fe_3O_4 counterparts. The following proves that covering with not magnetic compound reduces saturation magnetism. Despite deterioration, Ag–TeO_3/Fe_3O_4@TiO_2 encounters remarkable magnetic features that can be readily disconnected from the treatment by employing an eternal magnet [27].The reduction in magnetization of Fe_3O_4 after the formation of Ag/TeO_3@-Fe_3O_4/TiO_2 nanocomposites can be scientifically explained by the surface coating and incorporation of non-magnetic components. Pure Fe_3O_4 exhibits a high saturation magnetization due to the alignment of magnetic domains, but when coated with Ag/TeO_3 and TiO_2, a significant portion of the magnetic surface is shielded by these non-magnetic layers. This coating effect dilutes the overall magnetic response, leading to a measurable decrease in saturation magnetization. Quantitatively, the percentage loss in magnetization can be calculated using the formula

$$(\%)\ \text{loss} = \text{Ms}(Fe_3O_4)\text{-Ms}(\text{Ag-}TeO_3@Fe_3O_4\ /\ TiO_2)\ /\ \text{Ms}(Fe_3O_4) \times 100 \quad (2)$$

where, Ms represents the saturation magnetization of each sample. This calculation highlights the relative decline in magnetic strength caused by the non-magnetic coating, while still confirming that sufficient residual magnetization remains for efficient magnetic separation and recyclability of the nanocomposites. Therefore as -synthesized Ag–TeO_3@Fe_3O_4/TiO_2 have only 13.3 % loss of magnetization.

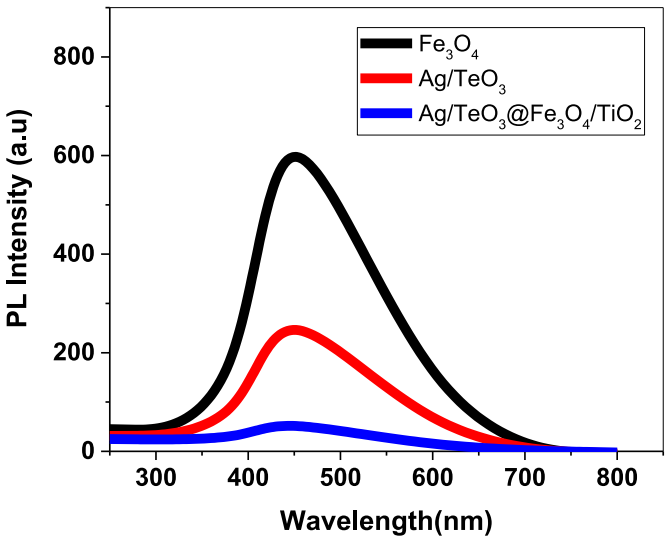


Fig. 8. PL spectra of Fe_3O_4, Ag/TeO_3, and $Ag/TeO_3@Fe_3O_4/TiO_2$ hybrid nanocomposites.

3.7. Morphological analysis

Fig. 7(a) shows the SEM profile of $Ag–TeO_3/Fe_3O_4@TiO_2$ NCs nanocomposites (NCs), revealing spherical nanoparticles with tightly bound structures. The TEM image in Fig. 7(b) reveals that the $Ag–TeO_3/Fe_3O_4@TiO_2$ nanocomposites possess a mixed morphology, where both larger and smaller spherical nanoparticles are uniformly distributed, and the phyto-molecule-assisted white layer indicates successful hybridization [28]. The average particle size of 8–12 nm confirms nanoscale dimensions favorable for enhanced surface reactivity. The SAED pattern in Fig. 7(c) displays distinct diffraction rings, validating the high crystallinity of the composite and its correspondence with the (101) plane of TiO_2. Furthermore, the HRTEM image in Fig. 7(d) demonstrates well-resolved lattice fringes, with interplanar spacings of 0.224 nm for Fe atoms and 0.318 nm for Ag atoms, which align with their respective crystal planes. These findings collectively confirm the crystalline, nanosized, and well-hybridized nature of the photocatalyst, essential for improved charge separation and photocatalytic efficiency.

3.8. Photoluminescence analysis

The photoluminescence (PL) spectra of Fe_3O_4, Ag/TeO_3, and $Ag/TeO_3@Fe_3O_4/TiO_2$ nanostructures highlight the influence of composite formation on charge carrier behavior as shown in Fig. 8. Pure Fe_3O_4 displays the strongest PL signal, reflecting a high recombination rate of photoinduced electron–hole pairs. When combined with Ag/TeO_3, the PL intensity decreases noticeably, indicating that Ag and TeO_3 promote charge separation by acting as electron sinks and minimizing recombination. The ternary $Ag/TeO_3@Fe_3O_4/TiO_2$ system exhibits the weakest PL intensity, signifying the most effective suppression of electron–hole recombination. This pronounced quenching effect arises from synergistic interactions and heterojunction formation between Ag/TeO_3, Fe_3O_4, and TiO_2, which enhance electron migration and extend carrier lifetimes. Thus, the PL results confirm that $Ag/TeO_3@Fe_3O_4/TiO_2$ achieves superior charge separation efficiency, directly contributing to its enhanced photocatalytic activity.

3.9. Photodegradation performance

The process of photocatalytic degradation of MB and MO dyes in aqueous solutions under ultraviolet (UV) light was examined using

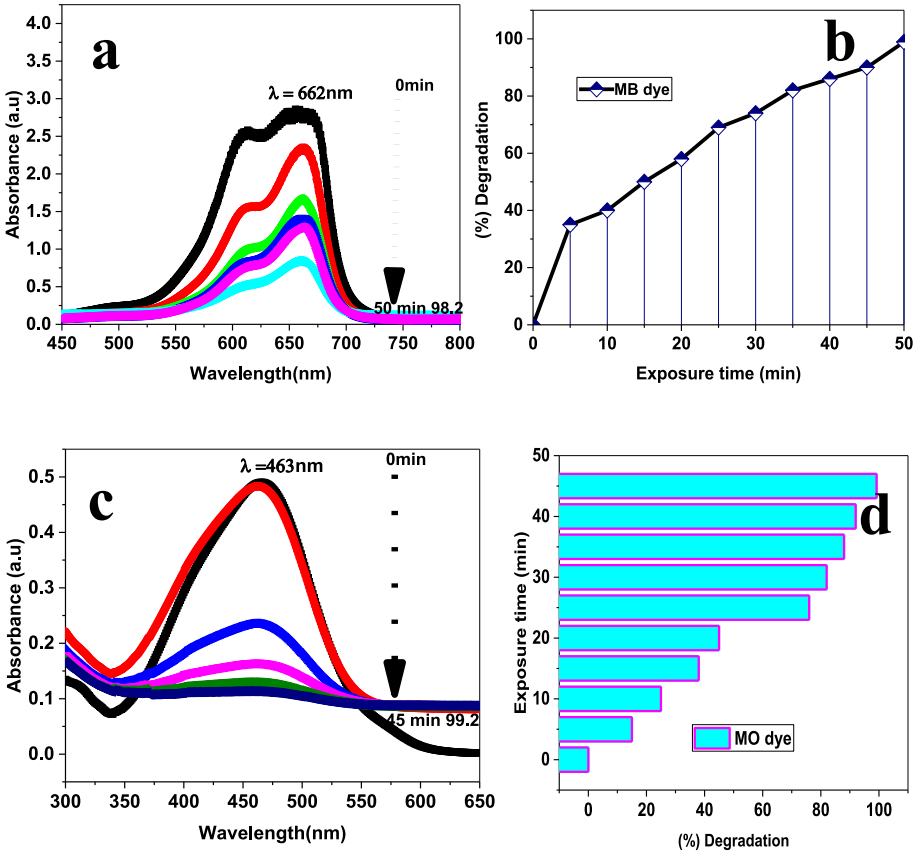


Fig. 9. (a) UV–Visible of MB dye degradation (b) (%) of MB dye degradation (c) UV–Visible of MO dye degradation (d) (%) of MO dye degradation.

Table 1
shows half -life period of MO and MB dye degradation.

s.no	Dye	R^2	K (min^{-1})	$t_{1/2}$ min
1	MO dye	0.99	0.0076	91.1
2	MB dye	0.98	0.0088	78.7

Table 2
Comparative table of photocatalytic degradation of Methyl orange and Methylene blue dye using different nanocatalyst.

S. No	Nanocatalyst	Light intensity	Time of exposure	References
1	$Ag/MoO_3/TiO_2$	350 W (Xe lamp)	95.6 % in 330 min	[34]
2	CdS Nanocrystal	18 W (LED-Vis-lamp)	95 % in 300 min	[35]
3	CTO/CN-1.0	300 W Xe lamp (λ > 400 nm)	70 % in 300 min	[36]
4	$[FemIL@SiO_2@Mag]_2MoO_4$	250 W (HP Hg lamp)	99 % in 30 min	[37]
5	$NiFe_2O_4/CoMoS_4$	250 W Xe lamp (λ > 420 nm)	99.0 % in 60 min	[38]
6	$Ag–TeO_3/Fe_3O_4@TiO_2$ NCs	400 W Hg lamp λ > 365 nm	50min 99.2 % 45min 98.2 %	Present work

$Ag–TeO_3/Fe_3O_4@TiO_2$ composite particles that featured a TiO_2 shell in thickness. Before performing experiments with these powders, preliminary control trials were conducted to account for the natural degradation of the dyes, ensuring that the data displayed in Fig. 9(a) and (c) represent degradation exclusively driven by photocatalysis. The degradation rate, represented as the relative dye concentration (C_0/C_t), was found to depend significantly on pH levels. The MB dye exhibited more efficient degradation under alkaline conditions (pH = 8), whereas the MO dye displayed greater degradation in acidic conditions (pH = 5). This difference arises primarily from the electrostatic interactions between the dye molecules and the surface charge of the composite particles in the aqueous medium [29].

As shown in Fig. 9(c), the composite particles possessed a positively charged surface in acidic environments (pH < 6), which promoted the adsorption of negatively charged MO dye molecules and thereby enhanced photocatalytic activity. On the other hand, the positively charged MB dye molecules were preferentially attracted to the negatively charged surface of the particles under basic conditions, facilitating degradation at pH = 8. Nonetheless, the rate of dye removal by these composite particles was slower than that achieved by the commercial Degussa P25 catalyst of equivalent particle weight. This slower performance is attributed to the presence of non-photocatalytic components, Fe_3O_4 and Ag–TeO in the composite particles, which contribute to the total particle weight during photocatalytic testing [30].

Notably, the photocatalytic efficiency is anticipated to improve as the thickness of the TiO_2 shell increases, up to a certain critical point. This improvement is primarily due to the higher proportion of semiconducting TiO_2, which generates free electrons and holes essential for redox reactions at the interface between the particle surface and dye molecules when exposed to UV light. However, if the shell thickness exceeds this critical threshold, the photocatalytic performance may either level off or diminish. This expected decline is based on observations that the specific surface area of the shell, rather than its thickness, becomes the dominant factor influencing photocatalytic efficiency. Comparative Table 2 shows that photocatalytic degradation of Methyl orange and Methylene blue dye using different nanocatalyst.

The Langmuir-Hinshelwood equilibrium framework is often employed for analysing the dynamics of multimodal photocatalytic breakdown was shown in Fig– 10(a). The given formula further shrinks

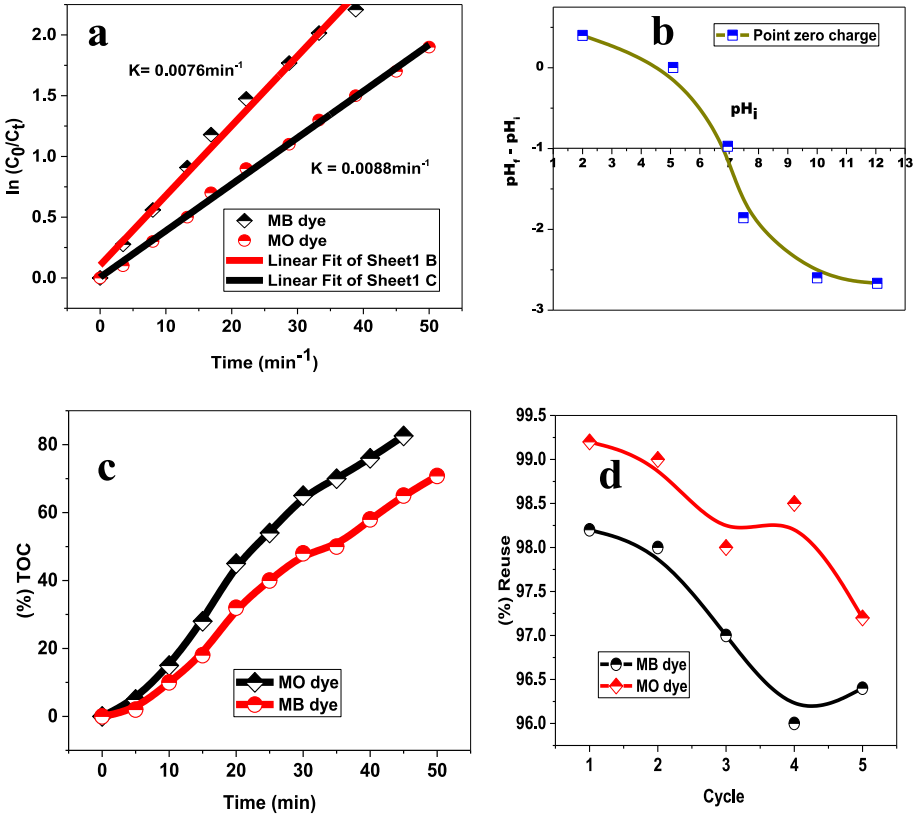


Fig. 10. (a) Kinetic approach (b) Zero-point charge (c) removal TOC (d) Regeneration test.

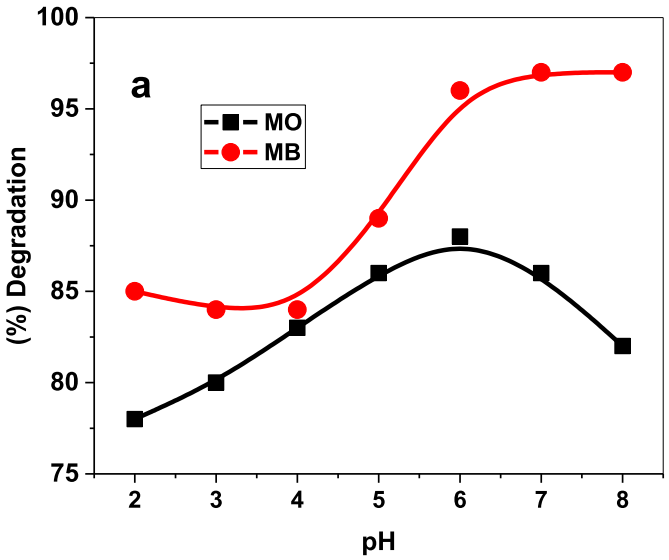


Fig. 11(a). Effect of pH of photocatalytic degradation of MB and MO over Ag–TeO_3/Fe_3O_4@TiO_2 nanocomposites.

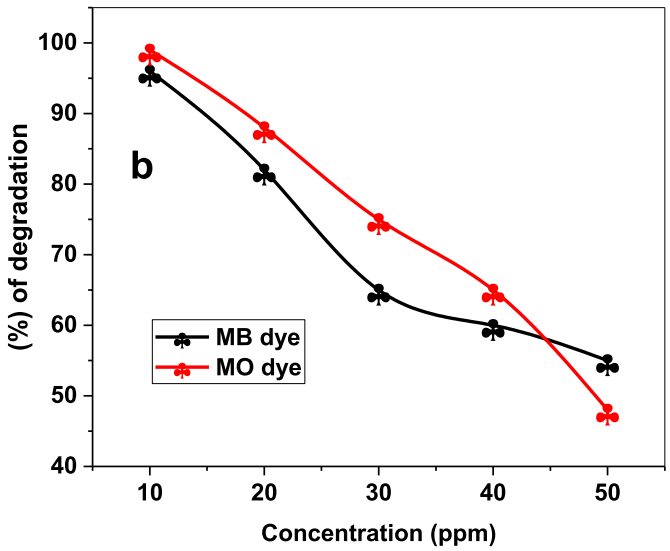


Fig. 11(b). Effect of initial concentrations of photocatalytic degradation of MB and MO over Ag–TeO_3/Fe_3O_4@TiO_2 nanocomposites.

towards pseudo-first order dynamics, yielding the resulting expression:

$$\mathrm{Ln}(C_0 / C_t) = -K_{app}t \quad (2)$$

where C_0 – Before degradation C_t – After degradation.

The coefficients of R^2 indicate that the photocatalytic breakdown is exponential that correlate with the Langmuir-Hinshelwood framework as represented in pseudo-first laws. The following Table 1 displays the momentum characteristics of MO photocatalytic break down, with the $t_{1/2}$ value computed assuming 0.693/k.

Fig. 10 (b) represents the pH is determined by the specific type of contaminant with the pHpzc, which indicates that the pH level upon the component's interface is equal overall or that the catalyst's exterior is completely neutral [31]. This pHpzc ratio needs to be examined to identify the optimal pH for a specific photocatalytic decomposition pathway. The point of equilibrium pH of Ag–TeO_3/Fe_3O_4@TiO_2 equals 6.7.

The role of adsorption and catalytic degradation in TOC removal can be clearly distinguished as shown in Fig. 10 (c). Adsorption primarily contributes to the initial reduction in dye concentration by physically binding organic molecules onto the surface of the catalyst; however, this process alone does not significantly decrease the total organic carbon, as the pollutants remain intact on the catalyst surface. In contrast, photocatalytic degradation plays the dominant role in TOC removal by utilizing photo-generated electron–hole pairs to produce reactive oxygen species (•OH and $\bullet O_2^-$), which oxidize the adsorbed dye molecules into smaller intermediates and ultimately mineralize them into CO_2, H_2O, and inorganic ions. This explains the substantial TOC reduction observed in this study, where MO and MB dyes showed 82.68 % and 70.8 % removal after 45 and 50 min, respectively, highlighting that adsorption supports pollutant capture, while catalytic degradation ensures complete breakdown and mineralization of organic content.

3.10. Optimization of photocatalytic degradation of organic dyes

3.10.1. Effect of pH

The photocatalytic degradation of MB and MO over Ag–TeO_3/Fe_3O_4@TiO_2 nanocomposites was studied as a function of pH, varying from 2 to 8, at an optimum catalyst dosage of 0.10 g and irradiation times of 50 min for MB and 45 min for MO. Solution pH plays a crucial role in determining the degradation efficiency, as shown in Fig. 11(a). The maximum degradation efficiencies were 97.43 % for MB at pH 8 and 88.4 % for MO at pH 6. The observed trend is explained by the point of zero charge (pH_pzc) of Ag–TeO_3/Fe_3O_4@TiO_2 nanocomposites, which is 6.7. When the solution pH exceeds the pH_pzc, the catalyst surface becomes negatively charged, favoring the adsorption and subsequent degradation of the cationic MB dye. Conversely, when the solution pH is below the pH_pzc, the catalyst surface is positively charged, which promotes the degradation of anionic MO dye through electrostatic attraction [32]. These findings are consistent with previous reports where modified chitosan-based photocatalysts exhibited similar pH-dependent behavior in dye removal. Thus, the results confirm that Ag–TeO_3/Fe_3O_4@TiO_2 nanocomposites can act as an efficient photocatalyst, with stronger activity toward MO degradation under acidic conditions and enhanced MB removal under alkaline conditions.

3.10.2. Effect of initial concentration of MB and MO dye

The effect of varying the initial dye concentration was studied by altering MB and MO levels from 10 to 50 mg/L, as shown in Fig. 11(b). An evident reduction in photocatalytic performance was noted with increasing concentration: MB degradation efficiency dropped from 98.6 % to 47.1 %, while MO decreased from 95.6 % to 54.9 %. This reduction is mainly due to the saturation of the photocatalyst surface, where the active sites of Ag–TeO_3/Fe_3O_4@TiO_2 nanocomposites are increasingly occupied by dye molecules, thereby limiting adsorption. In addition, higher dye concentrations hinder light penetration and create a shielding effect, which restricts the generation of hydroxyl radicals (•OH), the major reactive species responsible for oxidation [33]. Consequently, both radical formation and the overall photocatalytic efficiency diminish as dye concentration increases.

3.10.3. Reusability test

The catalyst's reuse ability has been assessed employing the identical way as that of the breakdown of photocatalytic catalysts. The Ag–TeO_3/Fe_3O_4@TiO_2 NCs were separated out employing a permanent attraction shortly after photocatalytic depletion, rinsed using alcohol and bottled water, evaporated in a heat source at 70 °C for 45 and 50 min, and retrieved for photo catalytic breakdown. This field study had to be done five-fold, with stimulus agility determined since the course of a cycle was shown in Fig. 10 (d).

The TEM images before and after five photocatalytic cycles confirm the reusability and structural stability of Ag–TeO_3/Fe_3O_4@TiO_2 during methyl orange and methylene blue degradation as shown in Fig. 12(a) and (b). Despite slight aggregation after repeated use, the overall morphology and framework remain intact, indicating minimal photo-

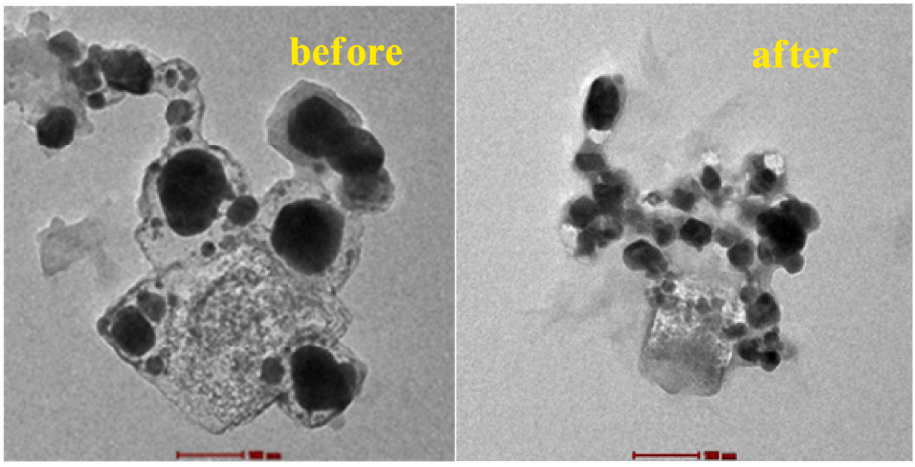


Fig. 12. (a) and (b) before and after treatment of photocatalytic degradation of methyl orange and methylene blue dye.

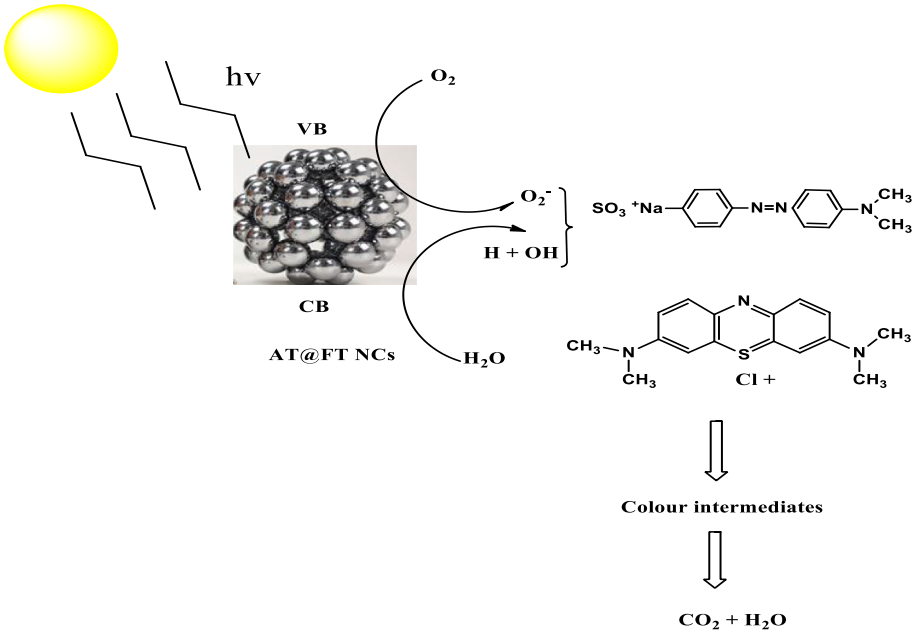


Fig. 13. plausible mechanism of MB and MO dye degradation.

corrosion or leaching. The TiO_2 support and strong interfacial bonding preserve crystallinity and stability, ensuring consistent photocatalytic efficiency and validating the nanocomposite's durability and recyclability for wastewater treatment.

3.10.4. Plausible mechanism

While UV rays strike the external layer of Ag–TeO_3/Fe_3O_4@TiO_2 NCs, photogenerated radicals and voids take place the plausible mechanism of MB and MO dye degradation as shown in Fig. 13. Fe^{3+} ions can capture electrons and holes, which leads to Fe^{2+} and Fe^{4+} ions, which have a less resilient than Fe^{3+} particles. Therefore, it prefers to revert to Fe^{3+}. Oxidation produces OH· radicals and O_2 anions. Despite the Ag Fermi density remains lower within TiO_2's conduction channel, the oscillating attractive particle orbiting Silver is triggered to a greater degree of energy. Consequently, it was capable of traveling to TiO_2's conduction region via hot electron injection, and these charged particles were then utilized to produce reactive oxygen species, thereby boosted photocatalytic capacity.

Photocatalytic processes tend to involve photo-excitation, separation of charges and movement, and interfacial oxidation-reduction reactions Photographic catalyst light generates reactive molecules such as h^+, OH^-, and O_2^-. To fully comprehend the structure of Fe and Ag breakdown of MO and MB dyes, it can be vital to determine that are reactive molecules perform a significant part in the photocatalytic dissolution processes. The OH· molecule is the most significant species that operates in photocatalytic combustion, is revealed by empirical studies, along with intermediates analytical results. OH radicals target the parallel and ortho locations of the rings made up of benzene due to their electrophilicity and electron-donating properties.

The electrons from the conduction band interact further with adsorbed molecular oxygen, generating superoxide ions (O_2^-). Simultaneously, Fe^{4+} ions engage with surface hydroxyl groups, resulting in the formation of hydroxyl radicals. Consequently, MO and MB dyes were degraded under UV light exposure. Moreover, the reduced semicircle diameter observed in the titanium nanocomposites, relative to bare TiO_2, indicated decreased resistance in interfacial charge transfer, enabling rapid electron movement and efficient separation of photo-induced charge carriers. This behavior was attributed to the excellent conductivity of the doped materials and the π–d interaction between the dopant and titanium, which significantly enhanced electron mobility

and charge separation, thereby inhibiting electron-hole recombination.

4. Conclusion

In conclusion, a green magnetic hybrid Ag–TeO_3/Fe_3O_4@TiO_2 nanocomposite was successfully synthesized and demonstrated excellent performance in photocatalytic dye degradation. Structural analysis by XRD confirmed a cubic spinel-like framework with TiO_2 in the anatase phase, while magnetic measurements showed a high saturation magnetization of 51.9 emu/g. The optical study revealed a narrow bandgap energy of 2.5 eV, supporting strong light absorption and charge transfer ability. Under UV irradiation, the nanocomposite achieved remarkable removal efficiencies of 99.2 % for methyl orange (MO) and 98.2 % for methylene blue (MB), following pseudo-first-order kinetics consistent with the Langmuir–Hinshelwood model. Importantly, the catalyst retained excellent recyclability, maintaining 96.4 % and 97.2 % degradation efficiency for MO and MB, respectively, even after five successive cycles. These results highlight the potential of Ag–TeO_3/Fe_3O_4@TiO_2 nanocomposites as a sustainable and reusable photocatalyst for wastewater treatment and effective elimination of organic pollutants.

CRediT authorship contribution statement

A. Anbu: Formal analysis, Data curation, Conceptualization. **M. Dilipkumar:** Formal analysis, Data curation, Conceptualization. **K. Jeyajothi:** Formal analysis, Data curation. **M. Rajasimman:** Validation, Supervision, Formal analysis, Data curation. **M.S. Manojkumar:** Validation, Formal analysis, Data curation.

Ethical approval

This declaration is not applicable.

Availability of data and materials

Data and materials will be made on request.

Funding

No financial assistance.

Declaration of competing interest

The authors declare that they have no known competing financial interests or personal relationships that could have appeared to influence the work reported in this paper.

Acknowledgement

This research obtained no financial assistance either from the general population, commercial reasons, or not-for-profit domains.

References

[1] H.S. Mazloomi Tabaei, M. Kazemeini, M. Fattahi, Preparation and characterization of visible light sensitive nano titanium dioxide photocatalyst, Sci. Iran. 19 (2012) 1626–1631.
[2] M. Safari, R. Talebi, M.H. Rostami, M. Nikazar, M. Dadvar, Synthesis of iron-doped TiO_2 for degradation of reactive orange 16, J. Environ. Health Sci. Eng. 12 (19) (2014) 1–8.
[3] Z. Mesgari, M. Gharagozlou, A. Khosravi, K. Gharanjig, Spectrophotometric studies of visible light induced photocatalytic degradation of methyl orange using phthalocyanine-modified Fe-doped TiO_2 nanocrystals, Spectrochim Acta A Mol. Biomol. Spectrosc 92 (2012) 148–153.
[4] M. Pazoki, M. Parsa, R. Farhadpour, Removal of the hormones dexamethasone (DXM) by Ag doped on TiO_2 photocatalysis, J. Environ. Chem. Eng. 4 (2016) 4426–4434.
[5] X. Jia, R. Dai, D. Lian, S. Han, X. Wu, H. Song, Facile synthesis and enhanced magnetic, photocatalytic properties of one-dimensional Ag@Fe_3O_4–TiO_2, Appl. Surf. Sci. 392 (2017) 268–276.
[6] N. Venkatachalam, M. Palanichamy, V. Murugesan, Sol–gel preparation and characterization of alkaline earth metal doped nano TiO_2: efficient photocatalytic degradation of 4-chlorophenol, J. Mol. Catal. A Chem. 273 (2007) 177–185.
[7] C.M. Teh, A.R. Mohamed, Roles of titanium dioxide and ion-doped titanium dioxide on photocatalytic degradation of organic pollutants (phenolic compounds and dyes) in aqueous solutions: a review, J. Alloys Compd. 509 (2010) 1648–1660.
[8] Y. Cheng, H. Sun, W. Jin, N. Xu, Photocatalytic degradation of 4-chlorophenol with combustion synthesized TiO_2 under visible light irradiation, Chem. Eng. J. 128 (2007) 127–133.
[9] J. Choi, S. Chung, K. Cho, K. Baek, S. Hong, D. Kim, S. Lee, Photocatalytic degradation of chlorophenol compounds using poly aromatic star copolymer, Water Air Soil Pollut. 223 (3) (2012) 1437–1441.
[10] C. Fàbrega, T. Andreu, A. Cabot, J. Ramon, Location and catalytic role of iron species in TiO_2:Fe photocatalysts: an EPR study, J. Photochem. Photobiol. A Chem. 211 (2010) 170–175.
[11] Q. Zhang, G. Meng, J. Wu, D. Li, Z. Liu, Study on enhanced photocatalytic activity of magnetically recoverable Fe_3O_4@C@TiO_2 nanocomposites with core–shell nanostructure, Opt. Mater. 46 (2015) 52–58.
[12] J.L. Wang, L.J. Xu, Advanced oxidation processes for wastewater treatment: formation of hydroxyl radical and application, Crit. Rev. Environ. Sci. Technol. 42 (2012) 251–325.
[13] C. Han, N. Zhang, Y.J. Xu, Structural diversity of graphene materials and their multifarious roles in heterogeneous photocatalysis, Nano Today 11 (2016) 351–372.
[14] H. Wang, W. Wan, Synthesis of Fe_3O_4/N–TiO_2/Ag hollow nanospheres and their application as recyclable photocatalysts, J. Cluster Sci. 27 (2016) 403–415.
[15] N. Zhang, M.Q. Yang, S. Liu, Y. Sun, Y.J. Xu, Waltzing with the versatile platform of graphene to synthesize composite photocatalysts, Chem. Rev. 115 (2015) 10307–10377.
[16] Y. Zhao, C. Tao, G. Xiao, G. Wei, L. Li, C. Liu, H. Su, Controlled synthesis and photocatalysis of sea urchin-like Fe_3O_4@TiO_2@Ag nanocomposites, Nanoscale 8 (2016) 5313–5326.
[17] J. Zhu, J. Ren, Y. Huo, Z. Bian, H. Li, Nanocrystalline Fe/TiO_2 visible photocatalyst with a mesoporous structure prepared via a nonhydrolytic sol–gel route, J. Phys. Chem. C 111 (2010) 18965–18969.
[18] Y. Mahmiani, A.M. Sevim, A. Gül, Photocatalytic degradation of 4-chlorophenol under visible light by using TiO_2 catalysts impregnated with Co(II) and Zn(II) phthalocyanine derivatives, J. Photochem. Photobiol. A Chem. 321 (2016) 24–32.
[19] M.Q. Yang, N. Zhang, Y. Wang, Y.J. Xu, Metal-free, robust, and regenerable 3D graphene–organics aerogel with high and stable photosensitization efficiency, J. Catal. 346 (2017) 21–29.
[20] U.G. Akpan, B.H. Hameed, Parameters affecting the photocatalytic degradation of dyes using TiO_2-based photocatalysts: a review, J. Hazard Mater. 170 (2009) 520–529.
[21] N.A. Jamalluddin, A.Z. Abdullah, Reactive dye degradation by combined Fe(III)/TiO_2 catalyst and ultrasonic irradiation: effect of Fe(III) loading and calcination temperature, Ultrason. Sonochem. 18 (2011) 669–678.
[22] V.N. Nguyen, N.K.T. Nguyen, P.H. Nguyen, Hydrothermal synthesis of Fe-doped TiO_2 nanostructure photocatalyst, Adv. Nat. Sci. Nanosci. Nanotechnol. 2 (2011) 035014.
[23] H.J. Kim, K.J. Jeong, D.S. Bae, Synthesis and characterization of Fe doped TiO_2 nanoparticles by a sol–gel and hydrothermal process, Kor. J. Mater. Res. 22 (2012) 249–252.
[24] A.D. Paola, G. Marci, L. Palmisano, M. Schiavello, K. Uosaki, S. Ikeda, B. Ohtani, Preparation of polycrystalline TiO_2 photocatalysts impregnated with various transition metal ions: characterization and photocatalytic activity for the degradation of 4-nitrophenol, J. Phys. Chem. B 106 (2002) 637–645.
[25] Y. Cong, J. Zhang, F. Chen, M. Anpo, D. He, Preparation, photocatalytic activity, and mechanism of nano-TiO_2 co-doped with nitrogen and iron(III), J. Phys. Chem. C 111 (2007) 10618–10623.
[26] J. Zhu, W. Zheng, B. He, J. Zhang, M. Anpo, Characterization of Fe–TiO_2 photocatalysts synthesized by hydrothermal method and their photocatalytic reactivity for photodegradation of XRG dye diluted in water, J. Mol. Catal. A Chem. 216 (2004) 35–43.
[27] T. Tong, J. Zhang, B. Tian, F. Chen, D. He, Preparation of Fe^{3+}-doped TiO_2 catalysts by controlled hydrolysis of titanium alkoxide and study on their photocatalytic activity for methyl orange degradation, J. Hazard Mater. 155 (2008) 572–579.
[28] A.D. Pomogailo, G.I. Dzhardimalieva, Thermolysis of metallopolymers and their precursors as a way for synthesis of nanocomposites, in: Nanostructured Materials Preparation via Condensation Ways, Springer, Berlin, 2014, pp. 287–388.
[29] L. Xu, J. Wang, Fenton-like degradation of 2,4-dichlorophenol using Fe_3O_4 magnetic nanoparticles, Appl. Catal. B Environ. 123–124 (2012) 117–126.
[30] S.E. Kim, J.Y. Woo, S.Y. Kang, B.K. Min, J.K. Lee, S.W. Lee, A facile general route for ternary Fe_2O_3@TiO_2@nanometal (Au, Ag) composite as a high-performance and recyclable photocatalyst, J. Ind. Eng. Chem. 43 (2016) 142–149.
[31] L. Xu, J. Wang, Magnetic nanoscaled Fe_3O_4/CeO_2 composite as an efficient Fenton-like heterogeneous catalyst for degradation of 4-chlorophenol, Environ. Sci. Technol. 46 (2012) 10145–10153.
[32] H.P. Li, J.Y. Liu, X.F. Liang, W.G. Hou, X.T. Tao, Enhanced visible light photocatalytic activity of bismuth oxybromide lamellas with decreasing lamella thicknesses, J. Mater. Chem. A 2 (2014) 8926–8932.

[33] E.D. Jeong, P.H. Borse, J.S. Jang, J.S. Lee, O. Jung, H. Chang, J.S. Jin, M.S. Won, H. G. Kim, Hydrothermal synthesis of Cr and Fe co-doped TiO_2 nanoparticle photocatalyst, J. Ceram. Process. Res. 9 (2008) 250–253.
[34] I.K. Konstantinou, T.A. Albanis, TiO_2-assisted photocatalytic degradation of azo dyes in aqueous solution: kinetic and mechanistic investigations: a review, Appl. Catal. B 49 (2004) 1–14.
[35] P.C. Dey, R. Das, Enhanced photocatalytic degradation of methyl orange dye on interaction with synthesized ligand-free CdS nanocrystals under visible light illumination, Spectrochim. Acta A Mol. Biomol. Spectrosc. 231 (2020) 118010.
[36] Q. Wang, Q. Guo, L. Wang, B. Li, The flux growth of single-crystalline $CoTiO_3$ polyhedral particles and improved visible-light photocatalytic activity of heterostructured $CoTiO_3$/g-C_3N_4 composites, Dalton Trans. 45 (2016) 17748–17758.
[37] A.G. Naikwade, M.B. Jagadale, D.P. Kale, A.D. Gophane, K.M. Garadkar, G. S. Rashinkar, Photocatalytic degradation of methyl orange by magnetically retrievable supported ionic liquid phase photocatalyst, ACS Omega 5 (2020) 131–144.
[38] N. Mukwevho, P.J. Mafa, K.K. Kefeni, A.K. Mishra, S.B. Mishra, A.T. Kuvarega, Photo-Fenton-like reaction for the degradation of methyl orange using magnetically retrievable $NiFe_2O_4$/$CoMoS_4$ heterojunction photocatalyst, J. Water Process Eng. 65 (2024) 105882.